Nanoscale Advances

Accepted Manuscript

This article can be cited before page numbers have been issued, to do this please use: X. H. Dao, H. K. Vu, T. H. Nguyen, M. T. Man, N. T. Giang, L. N. Nguyen, N. T. Tung, D. D. La, C. T. Nguyen and H. T. Nguyen, *Nanoscale Adv.*, 2026, DOI: 10.1039/D5NA01146A.

ROYAL SOCIETY OF CHEMISTRY

rsc.li/nanoscale-advances

View Article Online
DOI: 10.1039/D5NA01146A

ARTICLE

Enhanced Photocatalytic Activity of nano WO_3 via Thermal Plasma Treatment and Porphyrin Hybridization

Received 00th January 20xx,
Accepted 00th January 20xx

DOI: 10.1039/x0xx00000x

Xuan Huy Dao,†[a] Huu Khanh Vu,†[b,c] Thi Huyen Nguyen,[c,d] Minh Tan Man,[c,d] Thi Giang Nguyen,[b,c] Nhat Linh Nguyen,[b] Thanh Tung Nguyen,[b,c] Duc Duong La,[e] Cong Tu Nguyen[a] and Hoang Tung Nguyen*[b]

Surface modification of semiconductor photocatalysts is a frontier strategy for amplifying activity and facilitating advanced environmental applications. In this study, we demonstrate that tungsten trioxide (WO_3) nanoparticles subjected to surface engineering by DC thermal plasma, followed by hybridization with the Tetrakis (4-carboxyphenyl) porphyrin (TCPP) can yield a robust inorganic–organic hybrid with significantly enhanced photocatalytic activity in water treatment. The plasma process optimally tunes particle morphology and introduces abundant surface defects modulating bandgap energies and promoting superior charge separation, and substantially increasing the reactive surface area. Subsequent TCPP hybridization acts synergistically, leveraging the strong π-conjugation and light absorption of porphyrins to extend the photocatalyst's spectral response and foster interfacial charge transfer. Photocatalytic performance studies show that the hybrid material markedly outperforms either parent component alone, attaining rapid RhB degradation kinetics under visible light. This result is attributed to a combination of tailored surface area, engineered defect states, and organic–inorganic interfacial charge dynamics.

1. Introduction

The use of semiconductor materials in photocatalysis—the conversion of solar energy into chemical reactions—has recently gained attention as a potential method for cleaning up polluted environments and converting renewable energy sources. Given its non-toxicity, chemical stability, and advantageous band gap, tungsten trioxide (WO_3) has garnered considerable interest among these semiconductors.[1-3] However, its practical applications are often hindered by issues such as suboptimal light absorption, rapid electron–hole recombination, and limited active surface areas.[4-6]

Recent advances in plasma technology have opened new avenues for tailoring the physical and chemical properties of nanomaterials. Plasma-enhanced strategies can create high densities of surface vacancies, induce phase transitions, and alter particle morphologies, with direct consequences for surface reactivity and photocatalytic function.[7] The ability to fine-tune these features through process parameters such as plasma power, gas composition, and powder feed rate unlocks new opportunities for rational surface engineering.

In parallel, organic sensitizers like porphyrins have been widely studied for their strong visible light absorption and efficient charge transfer properties.[8] When combined with metal oxide semiconductors, porphyrin molecules can promote enhanced light harvesting and facilitate charge separation, thereby boosting photocatalytic efficiency.[9-12] While hybrid systems based on TiO_2 or ZnO have been widely explored, WO_3/porphyrin composites remain largely unstudied, despite the high potential of combining WO_3 with porphyrin light-harvesting capability. As far as our knowledge, no systematic study has investigated the surface modification of nano-WO_3 by thermal plasma, nor its subsequent hybridization with porphyrins for photocatalytic water treatment.

This work addresses these gaps by synthesizing nano-$WO_3{\cdot}H_2O$ via precipitation, subjecting it to DC thermal plasma treatment under varied feed rates, and subsequently hybridizing the plasma-modified WO_3 with tetrakis(4-carboxyphenyl)porphyrin (TCPP). The plasma treatment induced phase transformation and oxygen-vacancy formation, while simultaneously increasing surface area. When coupled with TCPP, the modified WO_3 demonstrated markedly enhanced photocatalytic activity, achieving up to 95% degradation of Rhodamine B (20 ppm, 20 mL solution) within 90 minutes using only 3 mg of catalyst. These results highlight that plasma-engineered WO_3 surfaces enable efficient organic–inorganic hybridization, yielding a synergistic photocatalyst with strong potential for environmental remediation.

[a] Faculty of Engineering Physics, Hanoi University of Science and Technology, Hanoi, Vietnam. Email: tu.nguyencong@hust.edu.vn
[b] Institute of Materials Science, Vietnam Academy of Science and Technology, Hanoi, Vietnam. Email: tungnh@ims.vast.ac.vn
[c] Graduate University of Science and Technology, Vietnam Academy of Science and Technology, Hanoi, Vietnam.
[d] Institute for Advanced Study in Technology, Ton Duc Thang University, Ho Chi Minh City, Vietnam.
[e] Institute of Chemistry and Materials, Hanoi, Vietnam
* Corresponding authors
† The authors contributed equally.

View Article Online
DOI: 10.1039/D5NA01146A

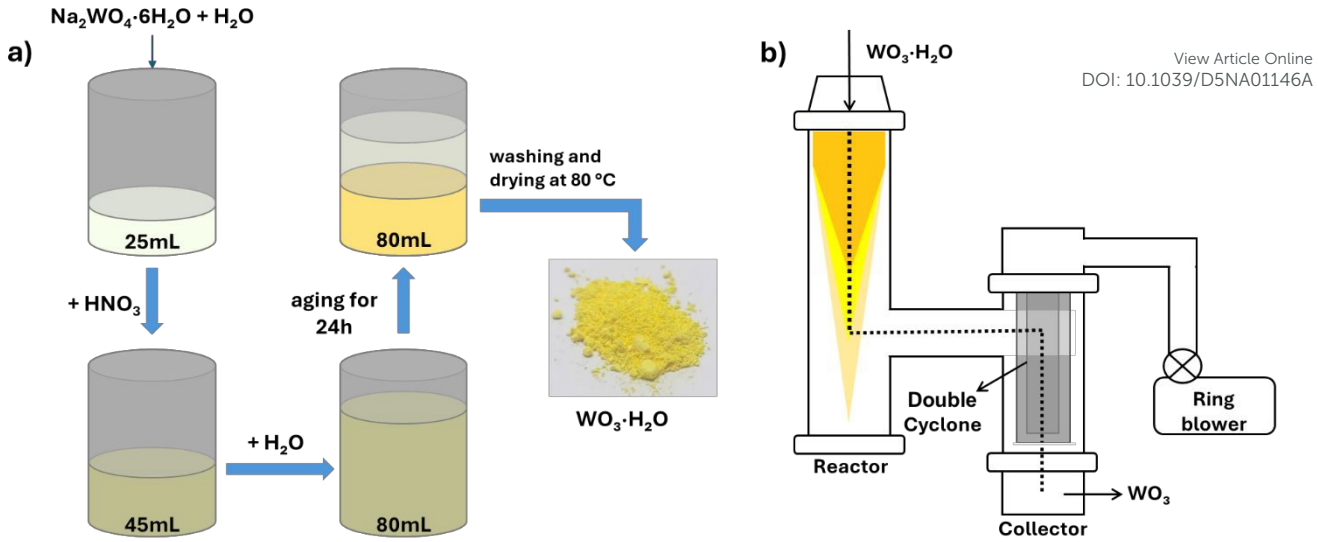

Fig. 1: Schematic of (a) $WO_3 \cdot H_2O$ fabrication and (b) thermal plasma treatment processes

2. Experiment details

2.1. Materials

Sodium tungstate dihydrate ($Na_2WO_4 \cdot 2H_2O$, 99.5%) and nitric acid (HNO_3, 37% wt.) were purchased from Xilong Scientific Co., Ltd. (China). Tetrakis (4-carboxyphenyl) porphyrin (TCPP), Sodium hydroxide (NaOH) and Hydrochloric acid (HCl) were purchased from Sigma Aldrich. Distilled water was used for all preparations.

2.2. Fabrication of $WO_3.H_2O$

The precursor $WO_3 \cdot H_2O$ material was synthesized via nitric acid precipitation method as follows. Initially, 8.25 g of $Na_2WO_4 \cdot 2H_2O$ was dissolved in 25 mL of deionized water while being stirred continuously for 15 minutes. After complete dissolution, 20 mL of HNO_3 was added dropwise with continued stirring for another 15 minutes. The solution was then diluted with deionized water to a total volume of 80 mL, resulting in a final pH of approximately -1. The mixture was stirred for an additional 2 hours and subsequently allowed to precipitate for 24 hours. The resulting precipitate was collected by filtration, washed thoroughly with deionized water, and dried at 80 °C.

2.3. Thermal plasma treatment of $WO_3 \cdot H_2O$

The material was dried prior to thermal plasma treatment. The $WO_3 \cdot H_2O$ nanoparticles were placed in a powder feeder connected to the reaction chamber, with the inflow rate controlled by adjusting the vibrating frequency from 60 to 70 Hz corresponding to the feeding rate from 8 g/min to 1.14 g/min. Nitrogen gas was employed both as the carrier gas (4 L/min) and as the main plasma gas, supplied through the upper electrode at a stable flow rate of ~80 L/min. The initial pressure inside the chamber was 615 Torr, with an applied current of 80 A and a voltage of 229 V, resulting in plasma power of approximately 18 kW.

The thermal plasma treatment process was carried out three times to investigate the material's changes under different feeding rates. The plasma-treated samples were labeled P01, P02, and P03, corresponding to the flow rates of 8 g/min, 4.37 g/min, and 1.14 g/min, respectively.

2.4. Synthesis of WO_3/TCPP

WO_3/TCPP porphyrins were synthesized via a self-assembly method (acid–base neutralization). TCPP was first dissolved in aqueous NaOH to form a clear solution. WO_3 samples - including nano $WO_3 \cdot H_2O$, P01, P02, and P03 - were then dispersed into the TCPP solution and subjected to ultrasonic agitation for 25 minutes to obtain solution A. Hydrochloric acid (HCl) was slowly added to solution A to neutralize the excess NaOH, adjusting the pH to approximately 6–7, resulting in solution B. Upon standing, solution B produced a green precipitate corresponding to the WO_3/TCPP hybrid composite, which was collected and used for further characterization and photocatalytic evaluation.

2.5. Characterisation methods

The XRD results were used to determine the crystal phase structure using an X-ray diffraction (XRD) pattern measured with an X'pert Pro Diffractometer (PANalytical MPD) employing Cu-Kα radiation with a wavelength of λ = 1.54065 Å, and a 2θ scanning range from 7° to 70°. The obtained XRD patterns were analyzed using HighScore Plus software in conjunction with the open-access ICDD database. Raman scattering spectra were measured using a Renishaw Invia Raman Microscope spectrometer with a laser source at a wavelength of 514 nm, enabling the investigation of surface characteristics of the materials. Diffuse reflectance and absorbance spectra were recorded using a UV-Vis JASCO 750 spectrophotometer, with a small amount of powder sample placed in the sample chamber and measurements taken in the wavelength range of 300–900 nm. SEM and EDX images were obtained using a Field Emission Scanning Electron Microscope (FESEM; Hitachi S-4800), operating at an accelerating voltage of 5 kV. X-ray photoelectron spectroscopy (XPS) was performed using a

View Article Online
DOI: 10.1039/D5NA01146A

Thermo K-Alpha+ spectrometer with an Al Kα X-ray source (spot size 400 µm), operating at a pass energy of 150 eV for survey scans and 50 eV for narrow scans with an energy step size of 0.1 eV and a dwell time of 50 ms under an ultimate vacuum of 5 × 10^{-8} mbar.

2.6. Photocatalytic studies

For the photocatalytic experiments, a solar-simulated system equipped with a 200W SX-TOB LED light source (24,000 lm, 6500 K) was used as the simulated sunlight system. The sample plane was positioned 20 cm below the lamp and the spectral distribution is shown in fig. S1. During testing, the photocatalyst suspension was continuously stirred with a magnetic stirrer to ensure homogeneous dispersion. The photocatalytic tests were conducted by placing 20 mL of 20 ppm RhB solution in a 50 mL beaker and adding 0.5 mL of the hybrid material suspension (equivalent to 3 mg of material), followed by vigorous stirring. The mixture was first placed in a dark environment for 10 minutes to achieve equilibrium before irradiation.[13] Then, at the time points of 5, 10, 20, 30, 45, 60, and 90 minutes, 2 mL of the solution was extracted, filtered, and analyzed using a USB4000 (Ocean optics) UV-Vis spectrophotometer. The RhB concentration was determined at the maximum absorption wavelength (λ_{max}) of 553 nm. The photocatalytic performance was estimated by calculating its efficiency (Equation (1)) based on the initial absorbance before illumination (C_o) and the absorbance after a selected degradation time (C).

$$\%Degradation\ efficiency = \frac{(C_0 - C)}{C_0} \times 100\% \quad (1)$$

3. Results and discussion

3.1. SEM analysis

The morphology of the nanomaterials before and after thermal plasma treatment was examined using scanning electron microscopy as presented in fig. 2(a) and figs 2(b-d), respectively. Since the activity of nanostructured photocatalysts is closely related to their shape and size,[14] morphological evaluation is critical. The pristine $WO_3 \cdot H_2O$ precursor presented in Fig. 2a appeared in sheet-like structures with relatively uniform thickness and smooth edges. In comparison to the precursor, the sample treated at the highest feeding rate (designated as P01) exhibited pronounced changes, the sheets changed to cubic and round shapes, forming larger clusters interspersed with smaller nanoparticles as seen in Fig. 2(b), which suggests

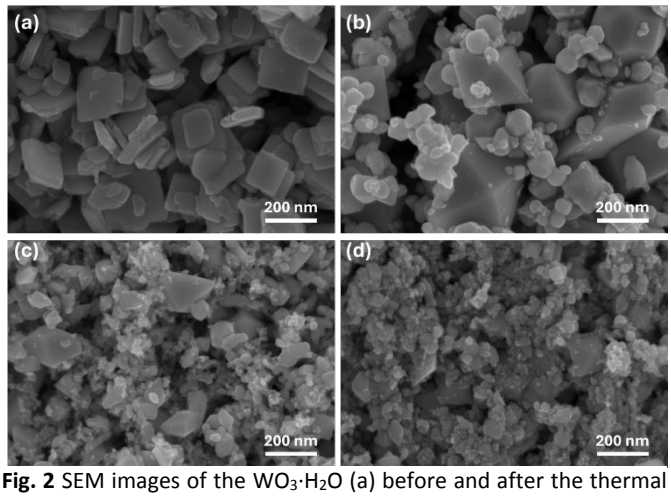

Fig. 2 SEM images of the $WO_3 \cdot H_2O$ (a) before and after the thermal plasma treatment as samples (b) P01, (c) P02, and (d) P03.

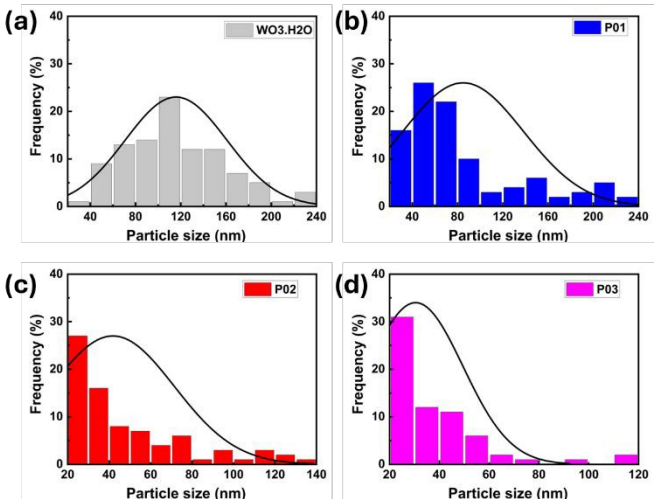

Fig. 3 Particle size analysis using ImageJ of (a) the $WO_3 \cdot H_2O$ precursor and the samples (b) P01, (c) P02, and (d) P03.

rapid thermal processing induces partial melting and restructuring. The P02 sample in Fig. 2(c), with a lower feeding rate, shows a reduction in the number of larger particles while smaller nanoparticles increases significantly, resulting in a decrease in average particle size. This trend continues by decreasing the feeding rate as seen in Fig. 2(d) for sample P03. The particle size was quantitatively analyzed using ImageJ software and is presented in fig. 3. The $WO_3 \cdot H_2O$ precursor exhibited the largest average particle size at approximately 115.86 nm, while the P01, P02, and P03 samples showed progressively smaller sizes of approximately 84.15 nm, 41.82 nm, and 30.44 nm, respectively, as detailed in Fig. 3 (a-d). The transformation from sheet-like precursor morphology to equiaxed nanoparticles, and the progressive size reduction from P01 to P03, can be attributed to the vaporization–nucleation–condensation–quenching mechanism inherent to DC thermal plasma processing. Upon injection into the plasma torch, the $WO_3 \cdot H_2O$ precursor particles are exposed to temperatures exceeding 2000 °C, completely destroying the original lamellar structure and converting the solid material into tungsten oxide vapor, from which isotropic nanoparticles subsequently nucleate and grow upon cooling. At high feed rates (P01), the elevated vapor concentration promotes frequent nucleus–nucleus collisions and heterogeneous condensation onto existing nuclei, resulting in coagulation-driven growth and larger particles; whereas at low feed rates (P03), the plasma energy is distributed over fewer particles, reducing vapor density and interparticle collision frequency, thereby generating a greater number of smaller, more uniformly distributed nuclei.[15] To further support these observations, BET

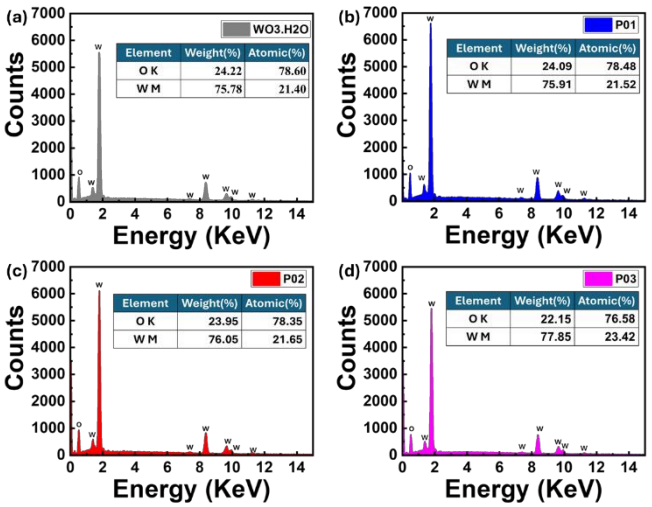

Fig. 4 EDX spectra of the $WO_3 \cdot H_2O$ precursor (a) and the samples P01 (b), P02 (c), and P03 (d)

surface area analysis was performed as presented in fig. S2. The raw $WO_3 \cdot H_2O$ precursor exhibited a surface area of 23.1 m^2/g, while plasma-treated samples showed progressively higher values: 33.6 m^2/g (P01), 47.6 m^2/g (P02), and 46.4 m^2/g (P03).

3.2. Elemental analysis

EDX spectroscopy was employed to analyze the elemental composition and assess the purity of the prepared samples. Figs. 4(a-d) present the spectra of the $WO_3 \cdot H_2O$ precursor and the samples P01, P02, and P03 obtained after thermal plasma treatment. Distinct signals corresponding to tungsten (W) and oxygen (O) were observed, indicating high purity with only minor variations in elemental ratios. The calculated O/W ratio exceeded 3 for all samples and exhibited a slight decrease as the plasma feed rate was reduced, suggesting progressive oxygen deficiency induced under more intense plasma exposure.

To clarify plasma-induced oxygen vacancies of the powders, the high-resolution W 4f spectrum of the plasma-treated P03 sample in fig. 5(a) clearly demonstrate the coexistence of W^{6+} and W^{5+}oxidation states. These correspond to the spin–orbit doublets of tungsten in different oxidation states. The splitting between the W $4f_{7/2}$ and W $4f_{5/2}$ components is ~2.1 eV, consistent with reported values for WO_3.[16] The peaks at 35.85 eV (W $4f_{7/2}$) and 38.01 eV (W $4f_{5/2}$) are assigned to W^{6+} species, while the lower binding energy peaks at 35.03 eV (W $4f_{7/2}$) and 37.06 eV (W $4f_{5/2}$) correspond to W^{5+} species. The presence of W^{5+} indicates partial reduction of tungsten, directly evidencing plasma-induced oxygen vacancies. These vacancies act as electron traps, enhancing charge separation and photocatalytic activity.

Complementary analysis of the O 1s region presented in fig. 5(b) further supports this conclusion. Two fitted peaks were observed at 530.61 eV and 531.90 eV. The lower-binding-energy peak at 530.61 eV is attributed to lattice oxygen bonded to tungsten (O–W), while the higher-binding-energy peak at 531.90 eV corresponds to oxygen-deficient regions (O vacancies).

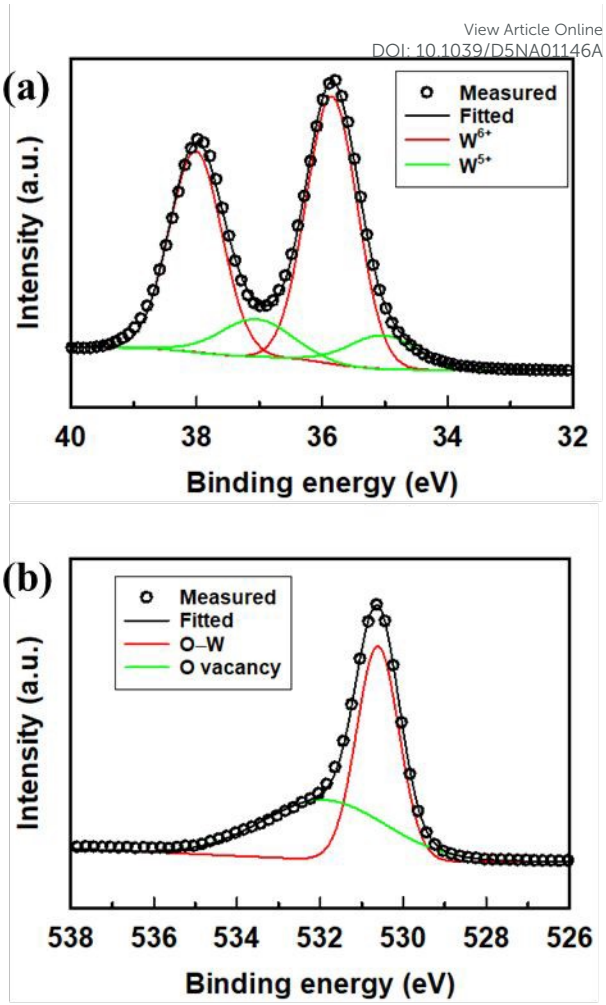

Fig. 5 XPS spectra of P03 for W 4f spectrum (a) and O 1s (b)

In addition to the XPS analysis of P03, the supplementary photographs of the powders (Fig. S3) provide a clear visual indication of plasma-induced modifications. The untreated $WO_3 \cdot H_2O$ precursor (a) appears as a bright yellow powder, consistent with its hydrated orthorhombic phase. After plasma treatment, the powders progressively change color: P01 (b) shows a pale green hue, P02 (c) a light blue, and P03 (d) a darker blue. Such color evolution is widely associated with the formation of oxygen-deficient tungsten oxides. The green-to-blue transition reflects partial reduction of W^{6+} to W^{5+}. Additional photoluminescence (PL) measurements (Supplementary Fig. S4) further support the role of plasma-induced oxygen vacancies. Plasma-treated samples exhibit stronger visible emission compared to the precursor, consistent with defect-related radiative recombination centers introduced by oxygen vacancies.[17]

3.3. XRD analysis

The crystal phase structure of the material after thermal plasma treatment was determined via X-ray diffraction (XRD) analysis (Fig. 6). The results revealed that the precursor $WO_3{\cdot}H_2O$ exhibited an orthorhombic structure, corresponding to standard card ICDD 01-084-0886. All three samples subjected to thermal plasma treatment exhibited a monoclinic WO_3 structure, in accordance with standard card ICDD 01-071-0305. Three prominent peaks observed at 23.06°, 23.53°, and 24.08° were assigned to the (002), (020), and (200) planes, respectively, which are characteristic of the monoclinic WO_3 phase.[18, 19] The near-identical peak positions and relative intensities of these patterns across the treated samples indicate that varying the feed rate did not affect the resulting crystal structure. It is evident that after plasma treatment, the samples underwent a complete phase transformation from orthorhombic $WO_3{\cdot}H_2O$ to monoclinic WO_3. The temperature at the tip of the thermal plasma spray torch in direct contact with the material is over 2000 °C. The treatment at elevated temperatures above 2000 °C is likely the primary factor driving the phase transformation.[20]

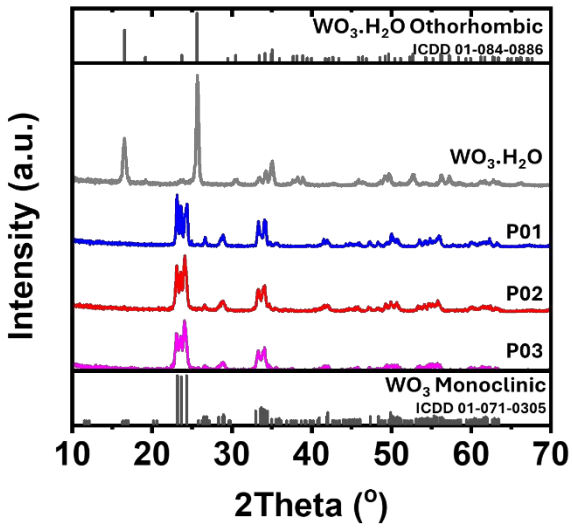

Fig. 6 XRD patterns of the samples

3.4. Raman scattering analysis

The Raman spectra of the precursor and plasma-treated materials are presented in fig. 7. For the precursor $WO_3{\cdot}H_2O$, the peak at 946 cm^{-1} is indicative of hydrated WO_3 and corresponds to the stretching vibration of the W=O bond.[21] Following the plasma treatment, the hydrated state of the material was completely eliminated, as indicated by the absence of the characteristic peak at 946 cm^{-1}. In the plasma-treated samples, characteristic Raman peaks of WO_3 were also observed. The peaks at 273 cm^{-1} and 716 cm^{-1} are attributed to the bending vibrations of W–O–W and O–W–O bonds, respectively, while the peak at 807 cm^{-1} corresponds to the stretching mode of the W–O–W linkage within the WO_3 crystal lattice. The peaks at 716 cm^{-1} and 807 cm^{-1} are recognized as signature features of monoclinic WO_3, consistent with the Raman spectrum of pure WO_3.[22] Furthermore, the changes in the intensity of the bands at 306, 677, and 716 cm^{-1} suggest that, in addition to the observed phase transformation, the feeding rate during the thermal plasma treatment also influences the internal bonding structure of the material.

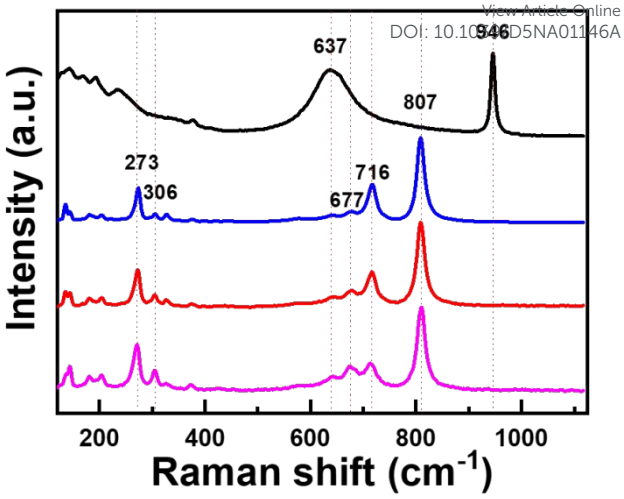

Fig. 7 Raman spectra of the $WO_3{\cdot}H_2O$ precursor and the thermal plasma-treated samples P01, P02, and P03.

3.5. DRS analysis

To evaluate the optical characteristics of the materials, diffuse reflectance spectra were also measured as shown in fig. 8(a). The diffuse reflectance of all three samples after thermal plasma treatment showed a significant decrease beyond 503 nm for samples P02 and P03, and beyond 512 nm for sample P01, compared to the $WO_3{\cdot}H_2O$ precursor. Furthermore, samples P02 and P03 exhibited lower reflectance than P01 in the wavelength range from 435 nm onward. This indicates that plasma treatment at lower feed rates enhances the material's light absorption capability. This trend suggests that plasma treatment helps to enhance optical absorption by modifying surface structure and defect density of the $WO_3{\cdot}H_2O$.

The optical bandgap (E_g) of the samples was estimated from the diffuse reflectance spectra using the derivative method derived from the Kubelka-Munk equation:[23]

$$\frac{d[\ln(F(R).h\nu)]}{d(h\nu)} = \frac{n}{h\nu - E_g} \quad (2)$$

In this equation, $F(R)$ is the reflectance function derived from the diffuse reflectance coefficient R, $h\nu$ represents the photon energy, and E_g is the optical bandgap of the material. The values n=2 and n=1/2 represent indirect and direct electronic transitions, respectively, as applicable to WO_3. The bandgap energy E_g is determined from the plot of $[\mathrm{d}[\ln(F(\mathrm{R}).h\nu)]/\mathrm{d}(h\nu)]$ versus $h\nu$, where the peak position indicates the transition energy.

The calculation results are presented in fig. 8(b). The orthorhombic $WO_3{\cdot}H_2O$ precursor exhibited a band gap of 2.37 eV, consistent with previously reported values.[24] In comparison, the bandgap of monoclinic WO_3 typically falls within the range of 2.5-2.8 eV.[25] After plasma treatment, the bandgap of the samples increased significantly, reaching 2.78 eV, 2.89 eV, and 2.91 eV for P01, P02, and P03 samples, respectively, with the bandgap widening progressively as the feed rate decreased. This blue shift in optical band gap is

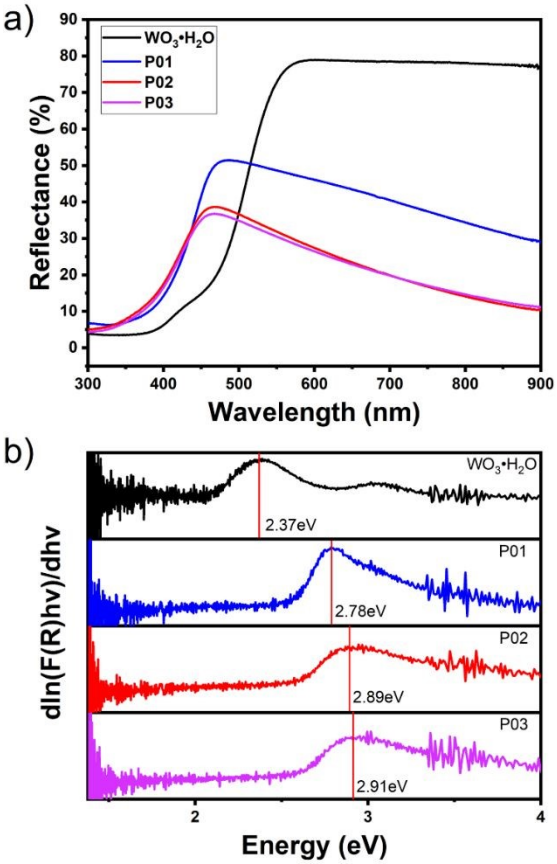

Fig. 8 UV-Vis spectra (a) and calculated band gap values of the samples (b).

attributed primarily to the plasma-induced phase transformation from hydrated orthorhombic $WO_3 \cdot H_2O$ to monoclinic WO_3, together with the introduction of oxygen vacancies and surface defects, which modify the electronic structure and optical absorption.[26]

3.6. SEM image of the composite material

The WO_3 samples including the $WO_3 \cdot H_2O$ precursor and the thermal plasma-treated samples were combined with TCPP nanofibers, the resulting composites were examined using SEM as shown in fig. 9. These TCPP nanofibers intertwine with WO_3 nanoparticles, creating a hybrid architecture. Fig. 9(a) displays the $WO_3 \cdot H_2O$/TCPP composite prepared from the untreated precursor, where the particles appear agglomerated and the presence of TCPP is not clearly discernible. In contrast, the samples P01/TCPP and P02/TCPP are shown in Figs. 9(b-c), where elongated rod-like structures corresponding to TCPP are evident, with WO_3 nanoparticles attached to their surfaces. Notably, the P02/TCPP sample features larger TCPP rods densely decorated with smaller WO_3 nanoparticles, exhibiting a relatively uniform distribution. Fig. 9(d) presents the P03/TCPP composite, in which ultra-small WO_3 nanoparticles nearly fully cover the surface of the TCPP rods, rendering the rod-like morphology less distinguishable. This progressive increase in WO_3 coverage correlates with the decreasing particle size resulting from lower plasma feed rates. These observations confirm the successful formation of WO_3/TCPP hybrid structures via a self-assembly process, with thermal plasma treatment playing a key role in tuning nanoparticle size and surface interaction with TCPP.

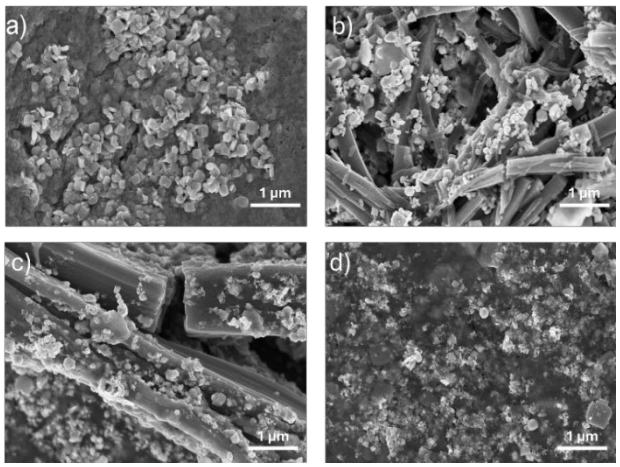

Fig. 9 SEM images of the $WO_3 \cdot H_2O$/TCPP composite (a) and the P01/TCPP (b), P02/TCPP (c), and P03/TCPP (d) samples.

3.7. Degradation of RhB

The photocatalytic activity of the prepared samples was evaluated by monitoring RhB degradation under simulated sunlight as presented in fig. 10. In this study, RhB was used at a concentration of 20 ppm, representing a moderately high dye load that challenges the photocatalytic efficiency of the materials. The $WO_3 \cdot H_2O$ precursor exhibited negligible photocatalytic activity after 90 minutes, confirming its limited efficiency in dye removal. In contrast, hybridization with TCPP led to a pronounced decrease in the absorption intensity of RhB at 553 nm, significantly enhancing photocatalytic efficiency for both the precursor and plasma-treated WO_3 samples. During the photocatalytic process, the absorption peak exhibits a blue shift toward shorter wavelengths, which is attributed to the presence of the organic compound porphyrins, consistent with previous reports.[27] To decouple the contributions of plasma treatment and TCPP sensitization to the overall photocatalytic performance, control experiments were conducted on plasma-treated WO_3 samples (P01–P03) without TCPP hybridization, and the results are presented in Supplementary Fig. S5. Under visible light irradiation, P01–P03 exhibit a distinctive adsorption-then-desorption profile: rapid RhB uptake occurs during the dark period and early irradiation, yielding high apparent removal, before the adsorbed dye is progressively released back into solution, with degradation efficiency returning to near zero by t = 30–90 min. This behavior confirms that plasma treatment markedly enhances the adsorption capacity of WO_3 through increased surface area and oxygen vacancy-rich surface chemistry, but is insufficient alone to sustain photocatalytic mineralization. This is in contrast to the untreated $WO_3 \cdot H_2O$ precursor shown in Fig. 10(a), which shows negligible adsorption and photocatalytic activity. Upon hybridization with TCPP, however, P01–P03 composites achieve sustained and progressively improving degradation efficiencies, confirming that TCPP sensitization is essential for converting the

View Article Online
DOI: 10.1039/D5NA01146A

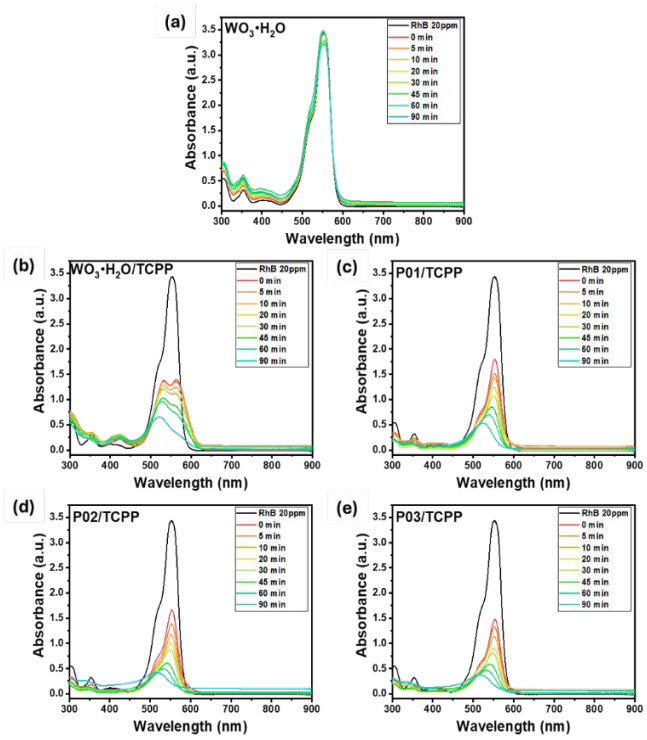

Fig. 10 Absorption spectra after the photocatalytic process of the precursor (a), $WO_3 \cdot H_2O$/TCPP (b), and plasma-treated WO_3 composites P01/TCPP (c), P02/TCPP (d), and P03/TCPP (e).

enhanced surface properties introduced by plasma treatment into effective and durable photocatalytic performance.

The absorption peak at 553 nm was used to calculate degradation efficiency as calculated in fig. 11(a) and the corresponding values after 90 minutes are summarized in Table 1.

Table 1. Degradation rate and linear fitting parameters

Catalyst	Degradation rate (%)	Slope
$WO_3 \cdot H_2O$/TCPP	73.57	0.00403
P01/TCPP	93.16	0.02154
P02/TCPP	94.04	0.02362
P03/TCPP	95.41	0.0252

The photocatalytic degradation efficiency of $WO_3 \cdot H_2O$/TCPP composite achieved a degradation efficiency of 73.57 % after 90 minutes, representing a substantial improvement over the pure $WO_3 \cdot H_2O$. Even higher efficiencies were observed for composites derived from plasma-treated nano WO_3, with P01/TCPP, P02/TCPP, and P03/TCPP achieving degradation rates of 93.16%, 94.04%, and 95.41%, respectively. These results demonstrate that thermal plasma treatment enhances the photocatalytic performance of WO_3/TCPP hybrids by more than 20% compared to the untreated $WO_3 \cdot H_2O$ precursor. This improvement confirms the successful formation of the composite material and its enhanced color removal efficiency.

Notably, even under high feed rate conditions, where the thermal plasma induces only a modest reduction in particle size, the photocatalytic properties of WO_3/TCPP composites improve significantly. This indicates that the beneficial effects of plasma

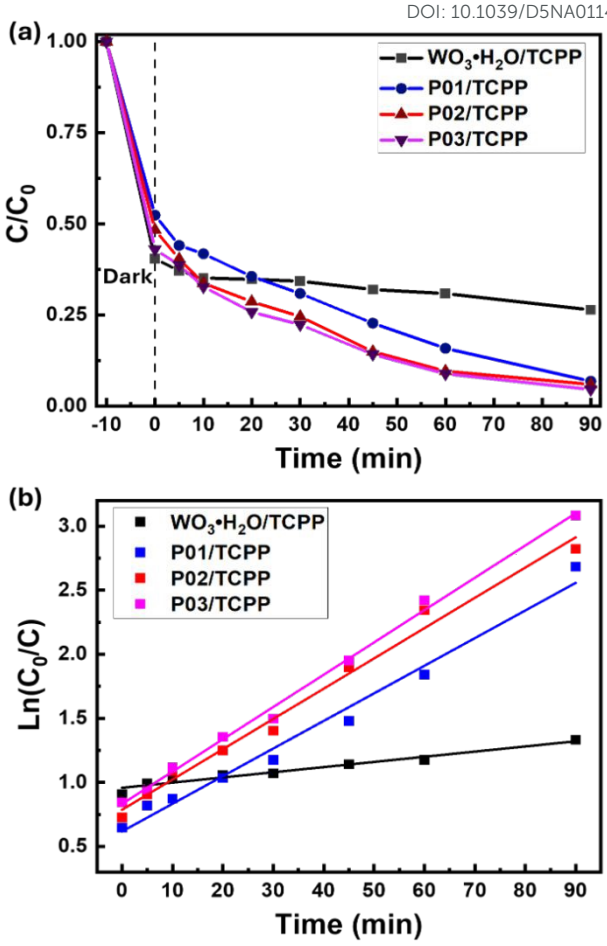

Fig. 11 Effect of treatment time on the RhB removal performances (a) C/C_0 plots of RhB solution and (b) ln (C/C_0) plots rate constant calculation of photoreactions

treatment are not limited to drastic nanostructural changes, but can be realized even with relatively mild processing. The enhancement can be attributed to plasma-induced surface restructuring and the generation of oxygen vacancies, which facilitate more efficient charge separation and stronger interaction with porphyrin molecules. These defect sites act as active centers for photocatalysis, enabling higher degradation rates despite only slight changes in particle size. Thus, while further reductions in feed rate yield progressively smaller nanoparticles and higher efficiencies, the catalytic activity does not increase proportionally. This indicates that defect generation plays a decisive role in performance enhancement. The dual contribution of particle size reduction and defect engineering underscores the versatility of thermal plasma treatment as a strategy for tailoring the photocatalytic properties of WO_3 and related semiconductor materials.

View Article Online
DOI: 10.1039/D5NA01146A

The degradation kinetics of RhB were further analyzed using pseudo-first-order reaction models as presented in fig. 11(b). The photocatalytic degradation process followed pseudo-first-order kinetics,[33] with the corresponding rate constants summarized in Table 1. Among the tested samples, the P03/TCPP composite exhibited the highest rate constant of 0.0252 min^{-1}, approximately six times greater than that of the $WO_3 \cdot H_2O$/TCPP composite. This kinetic enhancement aligns with the observed improvements in degradation efficiency and confirms the superior photocatalytic activity of plasma-engineered WO_3/TCPP hybrids.

Table 2 presents a comparative overview of photocatalytic degradation efficiencies reported for various WO_3-based materials. Most previously published systems rely on doping or complex composite strategies to enhance dye degradation. In contrast, the WO_3/TCPP composites synthesized in this study demonstrate remarkably improved performance under both visible light and simulated sunlight, highlighting the effectiveness of thermal plasma treatment as a scalable and adaptable method for photocatalyst development. Notably, the catalyst concentration employed in this work (0.15 g/L) is the lowest among all compared systems, and the dye concentration (20 ppm) is among the highest, representing a more demanding set of conditions than most reported studies.To assess the reusability and structural stability of the best-performing composite, three consecutive RhB photodegradation cycles were performed with P03/TCPP. The UV-Vis absorption spectra after each cycle are presented in Fig. 12(a), and the corresponding degradation efficiencies after 90 minutes are summarized in Fig. 12(b). The catalyst achieved degradation efficiencies of 95.41%, 94.25%, and 89.22% for cycles 1–3, respectively, retaining approximately 94% of its initial activity after three runs and confirming good operational stability. The modest reduction in efficiency across cycles is attributed to minor surface restructuring and partial active site blocking rather than fundamental degradation. To evaluate structural integrity, the surface morphology of P03/TCPP before and after three consecutive cycles was examined by SEM, as shown in Supplementary Fig. S6. The fresh catalyst (Fig. S6a) exhibits a relatively uniform distribution of WO_3 nanoparticles decorating the TCPP rod-like structures. After cycle 1 (Fig. S6b), slight

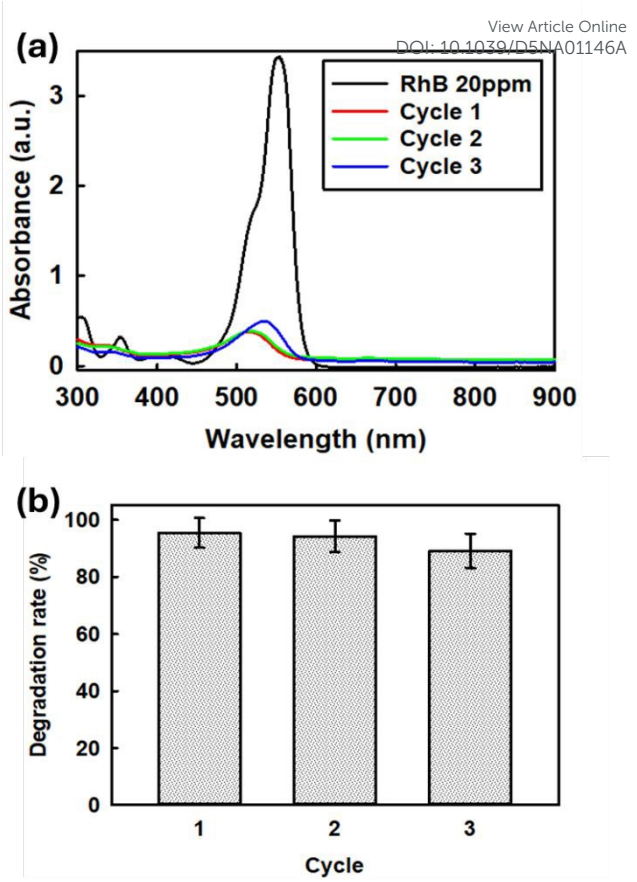

Fig. 12 Absorbance spectra of RhB solution after three consecutive photocatalytic cycles using P03/TCPP (a) and degradation efficiencies after 90 minutes for cycles 1–3 (b)

Table 2. Comparison of RhB photocatalytic degradation of other WO3-based photocatalysts with the investigated WO_3/TCPP

Catalysts	RhB concentration (ppm)	Catalyst loading	Volume (mL)	Light source	Irradiation time (min)	Degradation (%)	Ref.
WO_3@gC_3N_4	10	10 mg / 50 mL (0.2 g/L)	50	500 W Xe lamp	120	90	28
(Nb, Ta) doped WO_3	10	9 mg / 100 mL (0.09 g/L)	100	Visible light (unspecified lamp)	120	90.11	29
WO_3/AgBr	5	50 mg / 200 mL (0.25 g/L)	200	15 W daylight lamp	240	86	30
$NaNbO_3$/ WO_3	10	25 mg / 100 mL (0.25 g/L)	100	300 W Xe lamp, λ > 400 nm + ultrasound (180 W, 40 kHz)	120	73.7	31
Activated Carbon/WO_3	20	50 mL (0.25 g/L)	50	250 W Xe lam	300	88.59	32
WO_3/TCPP	**20**	**3 mg / 20 mL (0.15 g/L)**	**20**	**200 W LED solar simulator**	**90**	**95.41**	**This work**

particle aggregation and surface roughening are apparent, which become more pronounced after cycle 2 (Fig. S6c). After cycle 3 (Fig. S6d), the particles appear more compactly agglomerated, suggesting progressive surface restructuring during repeated use. Despite these morphological changes, the overall composite architecture remains recognizable and intact, consistent with the maintained photocatalytic performance. These results demonstrate that P03/TCPP possesses good photocatalytic stability and structural integrity over multiple cycles, establishing its suitability for repeated environmental remediation applications.

Conclusions

This study demonstrates that thermal plasma treatment is a highly effective strategy for transforming $WO_3 \cdot H_2O$ from its orthorhombic precursor into a monoclinic phase while simultaneously reducing particle size. These structural modifications, combined with the self-assembly of TCPP, result in the formation of WO_3/TCPP nanocomposites with exceptional photocatalytic performance, achieving up to 95.41% degradation of 20 ppm RhB dye under simulated sunlight within 90 minutes. The enhanced photocatalytic efficiency is attributed not only to the reduction in nanoparticle size but also to the increased defect density, particularly oxygen vacancies, introduced by high-temperature plasma exposure. These defects facilitate improved charge separation and broaden light absorption, contributing significantly to the overall activity. Furthermore, the systematic variation of feed rate during plasma treatment reveals a clear correlation between processing conditions, nanostructural evolution, and photocatalytic behavior. Notably, even at high feed rates, where particle size reduction is modest, the plasma-treated WO_3/TCPP composites exhibit substantial performance gains, underscoring the impact of defect engineering. These findings establish a versatile and scalable fabrication approach that integrates plasma processing with porphyrin sensitization, offering a promising pathway for the development of advanced photocatalysts in environmental remediation and sustainable energy applications.

Author contributions

XHD: investigation, data curation, writing – original draft; HKV: data curation, formal analysis, writing – review & editing; THN: investigation, visualization; MTM: validation; TGN: investigation, data curation; NLN: resources, data curation; TTN: supervision, funding acquisition; DDL: resources, writing – review & editing; CTN: conceptualization, resources, validation; HTN: conceptualization, supervision, writing – review & editing.

Conflicts of interest

There are no conflicts to declare.

Data availability

View Article Online
DOI: 10.1039/D5NA01146A

Data for this article are available at Zenodo at https://doi.org/10.5281/zenodo.17974589.

Acknowledgements

The authors would like to acknowledge the financial support from Vietnam Academy of Science and Technology, grant number NCXS02.02/25-26.

References

1. M. Liao, L. Su, Y. Deng, S. Xiong, R. Tang, Z. Wu, C. Ding, L. Yang and D. Gong, *Journal of Materials Science*, 2021, **56**, 14416-14447.
2. V. Dutta, S. Sharma, P. Raizada, V. K. Thakur, A. A. P. Khan, V. Saini, A. M. Asiri and P. Singh, *Journal of Environmental Chemical Engineering*, 2021, **9**, 105018.
3. H. Gao, L. Zhu, X. Peng, X. Zhou and M. Qiu, *Applied Surface Science*, 2022, **592**, 153310.
4. M. B. Tahir, G. Nabi, N. Khalid and M. Rafique, *Ceramics International*, 2018, **44**, 5705-5709.
5. F. Amano, E. Ishinaga and A. Yamakata, *The Journal of Physical Chemistry C*, 2013, **117**, 22584-22590.
6. D. S. de Sá, K. Leite dos Santos Castro Assis, C. C. de Mello, V. M. Paiva, M. F. Sampaio, O. C. Alves, A. M. da Silva, E. D´Elia, B. S. Archanjo and C. A. Achete, *Mater. Res. Bull.*, 2025, 113936.
7. S. Rahimnejad, J. H. He, F. Pan, X. e. Lee, W. Chen, K. Wu and G. Q. Xu, *Materials Research Express*, 2014, **1**, 045044.
8. Y. Huang, P. Zhao, H. Miao, S. Shao, L. Wang, Y. Chen, C. Jia and J. Xia, *Colloids and Surfaces A: Physicochemical and Engineering Aspects*, 2021, **616**, 126367.
9. M. E. Malefane, U. Feleni and A. T. Kuvarega, *New Journal of Chemistry*, 2019, **43**, 11348-11362.
10. M. E. Malefane, B. Ntsendwana, P. J. Mafa, N. Mabuba, U. Feleni and A. T. Kuvarega, *ChemistrySelect*, 2019, **4**, 8379-8389.
11. H. Zhu, W. Zhu, S.-Z. Kang, L. Qin, T. Zhang and X. Li, *Applied Surface Science*, 2024, **644**, 158783.
12. M. S. Khan, Y. Li, D.-S. Li, J. Qiu, X. Xu and H. Y. Yang, *Nanoscale Advances*, 2023, **5**, 6318-6348.
13. D. D. La, D. Nguyen and D. D. Nguyen, *Surfaces and Interfaces*, 2025, **59**, 105947.
14. M. B. Tahir, G. Nabi, T. Iqbal, M. Sagir and M. Rafique, *Ceramics International*, 2018, **44**, 6686-6690.
15. K. Park, Y. Hirayama and M. Shigeta, *Advanced Powder Technology*, 2025, **36**, 104793.
16. P. Chen, M. Baldwin and P. R. Bandaru, *Journal of Materials Chemistry A*, 2017, **5**, 14898-14905.
17. B. B. Wang, X. X. Zhong, C. L. He, B. Zhang, U. Cvelbar and K. Ostrikov, *Journal of Alloys and Compounds*, 2021, **854**, 157249.
18. J. Yang, X. Chen, X. Liu, Y. Cao, J. Huang, Y. Li and F. Liu, *ACS Sustainable Chemistry & Engineering*, 2021, **9**, 5642-5650.
19. I. Aslam, M. H. Farooq, M. Iqbal, R. Boddula, M. Abid, M. Ashfaq and U. Ghani, *Materials Science for Energy Technologies*, 2019, **2**, 187-193.

View Article Online
DOI: 10.1039/D5NA01146A

20. C. Y. Ng, K. A. Razak and Z. Lockman, *Electrochimica Acta*, 2015, **178**, 673-681.
21. Y. Zhang, Y. Shi, R. Chen, L. Tao, C. Xie, D. Liu, D. Yan and S. Wang, *Journal of Materials Chemistry A*, 2018, **6**, 23028-23033.
22. H. Guo, N. Jiang, H. Wang, N. Lu, K. Shang, J. Li and Y. Wu, *Journal of Hazardous Materials*, 2019, **371**, 666-676.
23. C. T. Nguyen, T. P. Pham, T. L. A. Luu, X. S. Nguyen, T. T. Nguyen, H. L. Nguyen and D. C. Nguyen, *Ceramics International*, 2020, **46**, 8711-8718.
24. P. Ou, F. Song, Y. Yang, J. Shao, Y. Hua, S. Yang, H. Wang, Y. Luo and J. Liao, *ACS omega*, 2022, **7**, 8833-8839.
25. R. Chatten, A. V. Chadwick, A. Rougier and P. J. Lindan, *The Journal of Physical Chemistry B*, 2005, **109**, 3146-3156.
26. Y. Qie, Z. Li, D. Wang, X. Bai, J. Fang, R. Liu, G. Wang, S. Zu, Y. Zhu and Y. Chen, *Journal of Alloys and Compounds*, 2024, **985**, 173725.
27. D. D. La, T. A. Nguyen, X. S. Nguyen, T. N. Truong, H. D. Ninh, H. T. Vo, S. V. Bhosale, S. W. Chang, E. R. Rene and T. H. Nguyen, *Journal of Environmental Chemical Engineering*, 2021, **9**, 106034.
28. P. Wang, N. Lu, Y. Su, N. Liu, H. Yu, J. Li and Y. Wu, *Applied Surface Science*, 2017, **423**, 197-204.
29. M. Pawar, P. Nain, S. Rani, B. Sharma, S. Kumar and M. M. Khan, *Optical Materials*, 2024, **157**, 116277.
30. J. Piriyanon, P. Takhai, S. Patta, T. Chankhanittha, T. Senasu, S. Nijpanich, S. Juabrum, N. Chanlek and S. Nanan, *Optical Materials*, 2021, **121**, 111573.
31. X. Yan, S. Zhang, L. Pan, T. Ai, Z. Li and Y. Niu, *Inorganic Chemistry Communications*, 2023, **158**, 111510.
32. K. Bhavsar, P. Labhane, V. Huse, R. Dhake and G. Sonawane, *Inorganic Chemistry Communications*, 2020, **121**, 108215.
33. N. Kannan, P. S. Venkatesh, M. G. Babu, G. Paulraj and K. Jeganathan, *Chemical Physics Impact*, 2023, **6**, 100230.

View Article Online
DOI: 10.1039/D5NA01146A

Data for this article are available at Zenodo at https://doi.org/10.5281/zenodo.17974589.